

Temperature dependent strengthening contributions in austenitic and ferritic ODS steels

S. Seils^{a,b}, A. Kauffmann^{a,*}, F. Hinrichs^a, D. Schliephake^a, T. Boll^{a,b}, M. Heilmaier^a

^a Institute for Applied Materials (IAM-WK), Karlsruhe Institute of Technology (KIT), Engelbert-Arnold-Str. 4, D-76131, Karlsruhe, Germany

^b Karlsruhe Nano Micro Facility (KNMF), Karlsruhe Institute of Technology (KIT), Hermann-von-Helmholtz-Platz 1, D-76344, Eggenstein-Leopoldshafen, Germany

ARTICLE INFO

Keywords:

ODS steels
Mechanical alloying
Microstructure characterization
Strengthening mechanisms
High temperature strength

ABSTRACT

We aim on the model-based description of the strength of ferritic and austenitic oxide dispersion strengthened (ODS) steels in the temperature range from room temperature (RT) up to 800 °C. Therefore, we present two approaches for the synthesis of austenitic alloys by mechanical alloying Y_2O_3 , namely with (i) elemental powders at RT and (ii) with a gas-atomized master-alloy. Consolidation of both powders by field assisted sintering technique leads to a more homogenous distribution of grain size and particles in specimens from elemental powders. In the entire temperature range, the compressive strength of the austenitic ODS steels is shown to be lower compared to the one of ferritic counterparts. Above approximately 500 °C, a strong decrease in strength is observed for all ODS variants due to the onset of creep-based deformation. Multi-scale materials characterization is performed to quantitatively assess microstructural materials parameters crucial for the modeling of the temperature dependent yield strength. These data are utilized to quantitatively describe the strength contribution by Hall-Petch and Orowan strengthening as well as dislocation strengthening at RT. Lower amounts of grain boundary and dislocation strengthening are found to be crucial for the lower strength of austenitic ODS steels. Meaningful calculation of materials strength is only achieved, when both interactions of strengthening contributions and experimental uncertainties are considered. Models describing diffusion-based creep (by Coble) and dislocation-based creep (by Blum and Zeng), which are shown to provide a more appropriate description of high temperature strength, are critically assessed for temperatures at and above the strength drop. It is shown that the deformation at high temperatures is possibly dominated by the formation and annihilation of dislocations at grain boundaries.

1. Introduction

Ferritic oxide dispersion strengthened (ODS) steels were introduced as promising materials for application at elevated temperatures in nuclear power generation [1,2]. Besides excellent resistance against swelling by exposure to radiation [3], they possess remarkable strength at room temperature (RT) and outstanding creep resistance above 600 °C as compared to non-ODS steels [1,2,4,5]. The origin of these characteristics is the presence of homogeneously dispersed, Y-Ti-O-type particles typically referred to as nanoclusters being less than 4 nm in size [4–10]. These nanoclusters result from the complex processing of ODS alloys, which includes mechanical alloying (MA) of elemental or pre-alloyed powders and subsequent consolidation [11–14]. Several consolidation techniques were used in literature, i.e. hot extrusion [1,2], hot isostatic pressing (HIP) [8,9], or more recently field assisted

sintering technique (FAST) [15]. Optionally, hot working is also applied in some cases to obtain semi-finished products such as rods, tapes, etc. [1,2,9].

In contrast to ferritic ODS steels, research on their austenitic counterparts just started in the last decade [16], even though they promise improved creep resistance due to their face-centered cubic (FCC) crystal structure. This closed-packed structure is typically associated with self-diffusion as well as diffusion of substitutional solutes being reduced by at least two orders of magnitude compared to open body-centered cubic (BCC) lattices [17]. Moreover, the higher Cr content further increases the corrosion resistance. Several austenitic ODS steels derived from the commercial non-ODS, austenitic steels AISI 304 [18–23], AISI 310 [24–26] and AISI 316 [27–34] have been investigated regarding their microstructural and mechanical properties. Nevertheless, a detailed discussion of the correlation between microstructure and

* Corresponding author.

E-mail address: alexander.kauffmann@kit.edu (A. Kauffmann).

<https://doi.org/10.1016/j.msea.2020.139452>

Received 21 January 2020; Received in revised form 22 April 2020; Accepted 22 April 2020

Available online 29 April 2020

0921-5093/© 2020 Elsevier B.V. All rights reserved.

strength is missing in most cases. Additionally, processing of austenitic ODS steels by MA revealed to be challenging, as a consequence of either the formation or the presence of the very ductile FCC phase. Hence, the powder tends to stick to the container walls and milling balls and often so-called process-control agents like alcohols are used to increase powder yield [26,27,36].

For this work, the ferritic ODS steel Fe-14Cr-0.4Ti-0.25Y₂O₃ (all compositions throughout the manuscript are given in wt.%) and an austenitic counterpart Fe-25Cr-20Ni-0.4Ti-0.25Y₂O₃ were manufactured by MA and subsequent consolidation by FAST. The composition of the alloys is derived from the widely investigated ferritic ODS steel 14YWT [37–39] and the non-ODS, austenitic steel AISI 310, respectively. To fundamentally study strengthening contributions, alloy compositions were kept as simple as possible. Thus, besides Cr and Ni (in the FCC case) only Y₂O₃ and Ti were added. Ti was added because of its crucial impact on the decrease in the size of nanoclusters [6].

In the case of ferritic ODS steels, temperature dependent yield strength has been analyzed with respect to particular strengthening mechanisms in the past already [5,39–42]. Several mechanisms were found to be relevant for the strength of the ODS steels. Besides the Peierls barrier to dislocation motion and solid solution strengthening, additional stress is necessary for dislocations to bypass nanoclusters, resulting in a significant Orowan strengthening (direct contribution). Furthermore, these nanoclusters prevent grain growth during consolidation by Zener-like pinning of grain boundaries, resulting in a sub-micron grain size [4] and remarkable Hall-Petch strengthening has been noted (referred to as indirect particle strengthening effect in Ref. [43]). Finally, due to MA, the initial powder particles undergo heavy deformation and, hence, exhibit high dislocation density prior to consolidation. During sintering recovery and possibly recrystallization occur, which lead to a reduction of the final dislocation density. Nevertheless, dislocation strengthening still has to be taken into account.

According to Refs. [44–47], a variety of superposition laws for the above described respective strengthening mechanisms i have been proposed which - depending on the strength and the density of obstacles - cover the entire range from root mean squared (rms) to linear superposition. Hence, the yield strength $\sigma_{0.2}$ is limited in between the two bounds as:

$$\sqrt{\sum_i \sigma_i^2} \leq \sigma_{0.2} < \sum_i \sigma_i \quad (1)$$

Above about $0.4 \cdot T_m$ (T_m is the melting temperature), creep-controlled deformation mechanisms become relevant and a substantial drop in yield strength [5,39] is typically observed for ODS steels. Influences due to coarsening of nanoclusters or grain size, respectively, can be excluded as several authors have proven the extraordinary stability of nanoclusters [38,48,49] as well as of the grain size [48,50] for long-term annealing at temperatures up to 1000 °C. Stable grain and particle sizes were also observed after annealing of the aforementioned austenitic ODS steels for 1000 h at 1000 °C, but are not further discussed in this work.

In the present work, we set up a model combining aspects of the low-temperature strength as well as the creep-related drop of strength at high temperature to describe the strength of the investigated ODS steels in the temperature range from RT to 800 °C. The proposed model is based on fitting (i) the superposition of various strengthening mechanisms at ambient temperature discussed in the context of Eq. (1) and (ii) the Coble diffusional creep model [51] or the alternative Blum and Zeng (BZ) dislocation based creep model [52,53] to experimental data. Both creep models might be relevant for the present case of sub-micron scaled, stable grain sizes at elevated temperatures with high grain boundary fraction, describing grain boundary diffusion controlled creep (Coble) and creep based on a dynamic equilibrium between annihilation and generation of dislocations at grain boundaries (BZ), respectively.

First, crucial materials parameters are determined and used for the calculation of the strengthening contributions. Since it is not easily possible to resolve the interaction of the strengthening mechanisms, the extreme values of the superposition are then calculated and critically assessed. Thereby, a special focus lies on the evaluation of uncertainties of strengthening contributions due to the intrinsic distribution of microstructural quantities such as grain size or particle size. Differences regarding the strength of ferritic and austenitic ODS steels are discussed. Finally, comparison of the high temperature strength data with the above-mentioned creep models allows the identification of probable creep mechanisms.

2. Experimental

All ODS steels investigated in this work were manufactured by powder metallurgical processing. The nominal compositions of the ferritic and austenitic ODS steels were Fe-14Cr-0.4Ti-0.25Y₂O₃ and Fe-25Cr-20Ni-0.4Ti-0.25Y₂O₃ (in wt.%), respectively. The so-called *ferritic* alloy was synthesized by MA of elemental powders of Fe, Cr and Ti (purity 99.2% or higher) with the addition of appropriate amounts of Y₂O₃ powder in a Simoloyer CM01 (Zoz GmbH) attritor under Ar atmosphere. Steel balls were used with a ball-to-powder ratio of 10:1 and the attritor was cooled to -20 °C. The net milling time was 60 h, while one milling cycle consisted of 45 s milling at 1000 rpm and 15 s cooling without rotation of the propeller. For the austenitic alloys two different processing routes were investigated similar to that suggested in literature. The first approach, designated *austenitic RT*, includes MA of elemental powders of Fe, Cr, Ni and Ti (purity 99.2% or higher) as well as Y₂O₃ powder in a PM400 (Retsch GmbH) planetary ball mill using WC balls (ball-to-powder ratio of 10:1) under Ar atmosphere. The net milling time was 4 h, while one milling cycle consisted of 60 s milling at 200 rpm and 120 s cooling without rotation. For the second approach, designated *austenitic CT* in what follows, a master alloy containing Fe, Cr and Ni (purity 99.2% or higher) was manufactured in an AM/0.5 arc melting furnace (Edmund Bühler GmbH) and subsequently gas atomized using N₂ in an Atomiser AU1000 device (at Indutherm Erwärmungsanlagen GmbH). The pre-alloyed Fe-25Cr-20Ni powder with powder particle size between 25 and 100 µm was MA with Ti and Y₂O₃ powder. Steel balls (ball-to-powder ratio of 10:1) and Ar atmosphere were used. The net milling time was 16 h. One milling cycle consisted of 15 min milling at 200 rpm and 15 min cooling with liquid N₂ and without rotation. Powders from the same alloy were mixed prior to further processing when milled in different containers in the planetary ball mill. MA at RT turned out to result in an insufficient powder yield. WC milling balls for cryo-milling led to significant wear and, thus, contamination of the powder with W, Co and C. In all milling trials no process control agent was used.

Consolidation of the powders was performed by means of field assisted sintering technique (FAST) in a Typ HP D device (FCT Systeme GmbH) at a temperature of 1100 °C and a load of 50 MPa for 5 min. Fast heating and cooling rates of 100 K/min were applied.

Compositions of the samples in the consolidated state were determined by inductively coupled plasma optical emission spectrometry (ICP-OES) for Y, hot gas extraction for O and N as well as spark optical emission spectrometry (spark OES) for all other elements. The compositions are summarized in Table 1. Metallographic sections perpendicular to the FAST compression direction were prepared by standard

Table 1

Chemical composition of the alloys determined by ICP-OES (+), hot gas extraction (*) and spark OES (°) (in wt.%).

Alloy	Fe ⁺	Cr ⁺	Ni ⁺	Ti ⁺	Y ⁺	O*	N*	C°
<i>ferritic</i>	bal.	11.9	0.13	0.38	0.16	0.46	0.05	0.24
<i>austenitic RT</i>	bal.	26.7	20.2	0.43	0.24	0.45	<0.01	0.12
<i>austenitic CT</i>	bal.	24.5	19.9	0.35	0.21	0.82	0.37	0.15

metallographic procedure using SiC grinding paper. Subsequent polishing with diamond suspensions down to 1 μm was applied. A final polishing step utilizing a non-crystallizing oxide suspension (pH = 9.8, Struers GmbH) was conducted to remove the surface-near deformation.

XRD analyses were carried out on polished sections using a D2 Phaser device (Bruker Corp.) equipped with a Cu X-ray source and a LynxEye line detector. To improve statistics, the samples were rotated during the measurement. Appropriate discriminator settings were used to filter fluorescence radiation of Fe and Ni. Backscatter electron (BSE) and electron backscatter diffraction (EBSD) analyses were performed using an Auriga 60 (Zeiss AG) scanning electron microscope (SEM). BSE images were taken at an acceleration voltage of 5–20 kV. EBSD analyses were performed on 70° pre-tilted samples. The acceleration voltage was 20 kV at working distances of 14–16 mm. Kikuchi patterns were collected with a DigiView camera (EDAX Inc.) and analyzed by the TSL OIM Data Collection software (EDAX Inc.). At least 4000 grains were analyzed for each condition with respect to their grain size and orientation by means of the TSL OIM software (EDAX Inc.). A minimum misorientation angle of 5° between neighboring pixels was used to identify grain boundaries [54]. Orientation maps were cleaned by means of the neighbor confidence index correlation method applied on data points with a confidence index CI < 0.1.

Tips for atom probe tomography (APT) were manufactured in a Strata dual beam SEM/focused ion beam (FIB) device by FEI. To avoid damage caused by the Ga^+ ion beam the region of interest was protected by a Pt layer first. Parts of an originally (30 × 4 × 3) μm^3 sized rod of the material are cut from the rod and set to Si micro-posts provided by Cameca SAS. Tips are shaped from the material by annular milling at 30 kV with decreasing inner diameter down to 0.2 μm . Final milling with a closed circular pattern is performed at 5 kV acceleration voltage to minimize the Ga^+ affected layer at the surface. Atom probe analyses were conducted in a LEAP 4000X HR atom probe (Cameca SAS). The device was operated in laser mode (UV laser with wave length $\lambda = 355$ nm) with a pulse energy between 50 and 100 pJ and a pulse repetition rate of 200 kHz. The temperature was set to 40 or 50 K and the standing high voltage was controlled by the detection rate set to 0.3–1%. Atom probe data were reconstructed and analyzed by IVAS 3.6.14 software (Cameca SAS). Particles were identified using the maximum separation method which is described in detail elsewhere [55–57]. As particle ions Y, YO, TiO, CrO and FeO were used. The necessary parameters d_{max} and N_{min} were determined for each tip following the description of Williams et al. [8]. Normally, d_{max} varied in the range of 0.6–1.8 nm and N_{min} was in the range from 6 to 30 ions. For l and d_{cr} the same value as for d_{max} was used. Subsequent to particle identification, a second refinement of the chemical results was performed using mass spectra of ions within the particle volume only. A significant deconvolution of formerly overlapping peaks in the mass spectra could be achieved. Identified nanoclusters contain between 46 and 56 at.% single Fe ions resulting from flight path aberrations due to a lower field of evaporation in the vicinity of the oxide nanoclusters [58]. Following Williams et al. [8], a matrix correction is applied to nanocluster data, which sets the content of single Fe ions in nanoclusters artificially to zero and reduces the content of single Cr and Ni ions proportionally to the alloy composition as well.

Mechanical properties were characterized in terms of compression tests in the temperature range from RT to 800 °C in air using a UPM-Zwick 1478 universal testing machine (Zwick GmbH) at an initial engineering strain rate of 10^{-4} s^{-1} . For that purpose, cylinders of 3 mm in diameter and 5 mm in height were cut by electrical discharge machining (EDM). The samples were ground to obtain parallel surfaces and BN spray was applied to reduce friction during testing. Inductive heating of the samples to the requested temperature for at least 20 min prior to testing was performed. Long-term annealing tests have shown that neither the grain size nor the nanocluster size changes at temperatures up to 1000 °C. Strain gauges attached to the compression dies in direct vicinity to the samples were used to determine the strain. An engineering, compressive strain of at least 7% was achieved in all cases.

Yield strength $\sigma_{0.2}$ was obtained from the stress-strain curves at 0.2% plastic deformation.

3. Results and discussion

3.1. Processing of austenitic ODS steels

Fig. 1a and b shows the formation of a single-phase austenitic matrix after consolidation on a macroscopic length scale independent from processing elemental or pre-alloyed powders. For better visibility of small diffraction peaks, the intensity scale of the diffraction patterns in Fig. 1a and b is plotted logarithmically. Identified peaks (closed triangles) correspond to FCC Cu-prototype, while no oxide peaks were observed. The lattice parameters of both austenitic alloys (*austenitic RT* and *CT*) are comparable to the lattice parameter of the arc-melted and gas atomized master alloy which is 3.592 Å (not shown here). This is slightly larger than a reported lattice parameter for AISI 310 which is 3.582 Å [59]. Given the tolerance level regarding contamination in the standard, this difference is not significant. From the BSE image of *austenitic RT* (Fig. 1c), a homogeneous distribution of sub-micron sized grains can be expected. In contrast, *austenitic CT* (Fig. 1d) consists of regions with fine or coarse grains. Agglomerations of coarse particles (parts of large carbides were detected in some APT tips) are visible in the magnified BSE images (insets of Fig. 1c and d). They are remarkably larger than the expected nanoclusters and appear as bright (flare contrast in BSE images) or dark (chemical contribution to BSE images) spots in the microstructure. Particle sizes (about 60 nm) and volume fraction (about 1%) were roughly estimated by optical analysis (ImageJ) for both alloys and, hence, a contribution of these particles to yield strength is negligible. Nevertheless, the grain size in regions of coarse particle agglomerations is found to be smaller compared to regions with lower coarse particle density and, thus, it is supposed that these particles hinder grain growth. Furthermore, it was found in APT analysis that coarse grained regions of *austenitic CT* are free from nanoclusters. Due to this inhomogeneity in grain size and nanocluster distribution, we conclude that the processing of austenitic ODS steels from elemental powders (*austenitic RT*) is preferred over starting with pre-alloyed powders (*austenitic CT*). The major contribution to this difference is most probably arising from the entire ductile behavior of the pre-alloyed, fully austenitic starting material which is obviously not sufficiently suppressed by the cryogenic milling conditions in *austenitic CT*. Furthermore, this inhomogeneity cannot be easily described in the models to compare the temperature dependent strength of ferritic and austenitic ODS steels. Therefore, *austenitic CT* is not further discussed in the following.

3.2. Microstructural characterization

For the calculation of the strengthening mechanisms, it is necessary to determine the following microstructural parameters: dislocation density ρ_{dis} , grain size d_{g} , and nanocluster size d_{p} as well as the nanocluster density ρ_{p} .

A normalized Williamson-Hall (WH) plot derived from XRD patterns of the *ferritic* alloy and *austenitic RT* is depicted in Fig. 2 separating the contributions from ρ_{dis} and the size of coherently scattering domains to the total width of the diffraction peaks. While other experimental methods to determine ρ_{dis} (e.g. transmission electron microscopy or EBSD) can only identify fractions of all dislocations present in the material, only XRD allows for the analysis of geometrically necessary as well as statistically stored dislocations. Instrumental line broadening is corrected by subtracting the peak width data of a LaB₆ powder sample from the original data. Peak broadening is determined from the full width at half maximum (FWHM) of the peaks. The respective peak widths in the WH plot do not lie on a straight line due to the anisotropy of peak broadening. As a first approximation, the elastic anisotropy is

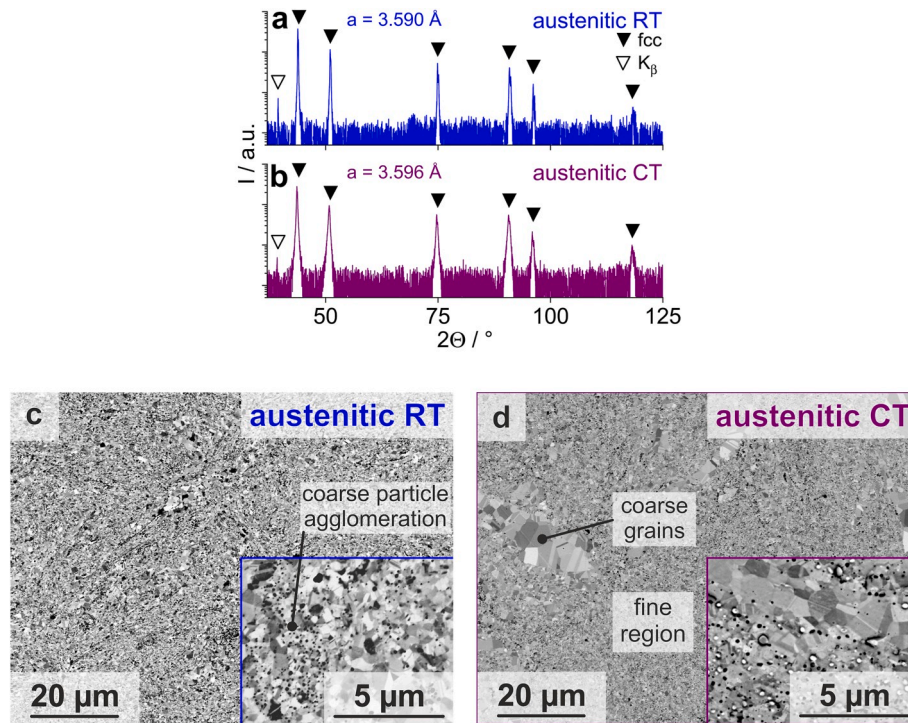


Fig. 1. XRD patterns of a) *austenitic RT* and b) *austenitic CT* and corresponding micrographs in c) & d) after consolidation by FAST. Closed triangles in the XRD patterns highlight peak positions calculated from lattice parameter for the austenite. Open triangles highlight residual K_{β} peaks. The BSE images in c) & d) exhibit combined chemical and orientation contrast. Insets in c) & d) show coarse particles in the materials.

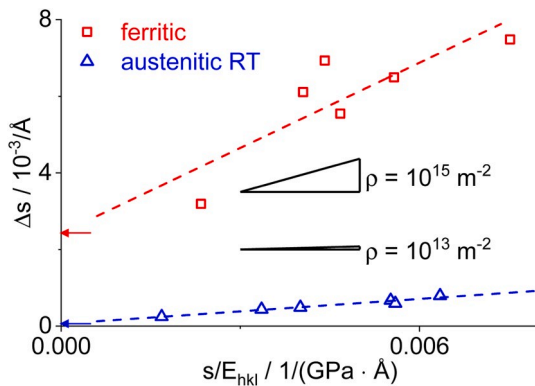


Fig. 2. E_{hkl} -normalized Williamson-Hall plot of *ferritic* and *austenitic RT* after consolidation. Arrows indicate intercepts used to determine the sizes of coherently scattering domains, which are 0.037 and 1.461 μm for *ferritic* and *austenitic RT*, respectively.

corrected by dividing the scattering vectors by the direction-dependent (hkl) Young's modulus E_{hkl} [60]. Gradient triangles show the expected slope in the WH plot for dislocation densities ρ_{dis} of 10^{13} and 10^{15} m^{-2} , respectively. Table 2 summarizes all obtained microstructural parameters. Given error ranges for ρ_{dis} represent the error propagation from the uncertainty of the slope determination in the E_{hkl} -normalized WH plot. ρ_{dis} of the *ferritic* alloy is almost two orders of magnitude higher than in *austenitic RT*. Note that the dislocation density of *ferritic* as well as of *austenitic RT* was in the range of 10^{16} m^{-2} prior to consolidation. Hence, the lower dislocation density of *austenitic RT* results, to a substantial extent, from an increased annihilation of dislocations during consolidation by recovery and/or by recrystallization. Furthermore, it is anticipated that the given dislocation densities represent an upper limit for the respective materials since the calculation implies that the entire lattice distortion traces back to dislocations and further contributions

Table 2

Summary of the microstructural parameters for the calculation of strengthening contributions determined by XRD ($^+$), EBSD (*) and APT ($^{\circ}$) analysis.

microstructural parameter	unit	<i>ferritic</i>	<i>austenitic RT</i>
ρ_{dis}^+	10^{15} m^{-2}	3.2 ± 2.1	0.08 ± 0.02
a^+	Nm	0.2875 ± 0.0001	0.3590 ± 0.0002
d_g^*	μm	0.75 ± 0.66	0.43 ± 0.27
d_p°	nm	5.0 ± 3.2	2.8 ± 2.2
ρ_p°	10^{22} m^{-3}	1.2 ± 0.8	5.6 ± 5.0

due to particles and solutes are neglected.

Additionally, from the intersection with the Δs -axis, the size of coherently scattering domains is estimated correlating with the (sub-) grain size in the material. The determined grain sizes are 0.037 μm and 1.461 μm for the *ferritic* alloy and *austenitic RT*, respectively. They differ remarkably from grain sizes determined by EBSD analysis, see Table 2. Coherent scattering domains can be confined by other lattice defects than high angle grain boundaries as well. In the further course of the present article, a description of Hall-Petch strengthening is performed. Since high angle grain boundaries impermeable to dislocation motion are assumed to be operative in this case, grain sizes determined by EBSD are preferred throughout the article.

EBSD orientation mappings of *ferritic* (Fig. 3a) and *austenitic RT* (Fig. 3b) exhibit a homogeneous, unimodal distribution of sub-micron sized grains. The orientation maps do not show preferential crystal orientations for the *ferritic* alloy. Slightly preferential orientation of grains with [110] direction parallel to the compression direction (max. multiples of the uniform distribution of about 2) is found for *austenitic RT*. Crystallographic texture is negligible for strength evaluation if present at all. Table 2 gives the mean area weighted grain sizes, while Fig. 3c shows relating area weighted grain size distributions obtained from EBSD orientation mappings. The mean grain size of *austenitic RT* was found to be only half that of the *ferritic* alloy. Area weighted grain

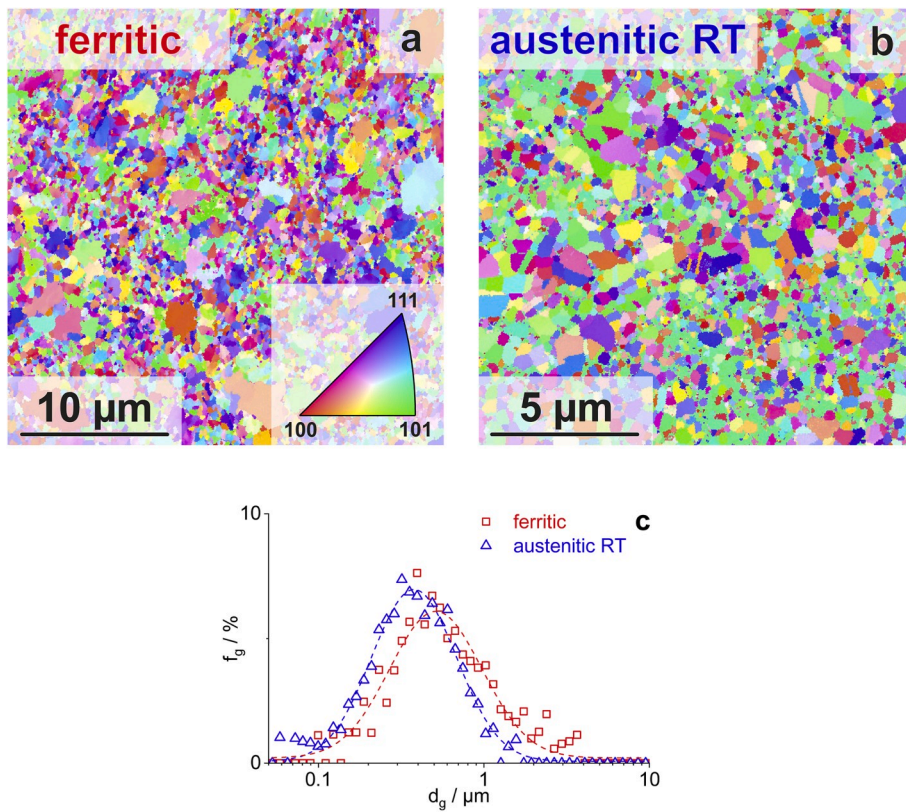


Fig. 3. Orientation mappings by EBSD of a) *ferritic* and b) *austenitic RT* color-coded with respect to the inverse pole figure (inset in a) of the compression direction during FAST (compression direction is perpendicular to the image plane). c) shows the area weighted grain size distribution obtained from the EBSD orientation maps (dashed lines according to the log-normal distributions are added to guide the eyes). (For interpretation of the references to color in this figure legend, the reader is referred to the Web version of this article.)

sizes are used due to their relevance for mechanical properties, e.g. on Hall-Petch strengthening.

The sections of atom probe datasets in Fig. 4a and b shows Y–Ti–Cr–Fe–O-containing nano-sized particles hereafter called nanoclusters in all of the investigated samples. The reconstructions typically represent sections of 30 nm in thickness and 250 nm in length. For the sake of clarity, only particle forming ions, namely Y, YO, TiO, CrO and FeO, are displayed in these reconstructions. Other elements like Fe, Cr and Ni are homogeneously distributed throughout the tips and are, therefore, omitted.

Fig. 4c shows a broad distribution in particle size d_p for the investigated alloys ranging about two orders of magnitude. For the calculation of mean values and standard deviations of d_p as well as to obtain the particle size distribution all particles found in several tips of the same alloy (at least 150 particles in total) were summarized and the results are given in Table 2. Since the analysis direction of the atom probe tip is less

affected by flight path aberrations [61], d_p is defined as twice the radius of gyration in this direction. Mean values and standard deviations of particle densities ρ_p (Table 2) were calculated on the basis of particles found in each analyzed atom probe tip of the same alloy. The resulting standard deviation is comparably high as APT investigations revealed an inhomogeneous distribution of particles in the material. The atom probe analysis shows that independent from the different processing of ferritic and austenitic alloys, nanoclusters with less than 10 nm in size are formed in both types of material.

3.3. Mechanical properties at room temperature

To investigate mechanical properties at RT, compression tests were conducted on the *ferritic* alloy as well as on *austenitic RT*. Since no significant preferential orientation of grains was observed after FAST, no anisotropy of the compressive strength is expected. Nevertheless, the

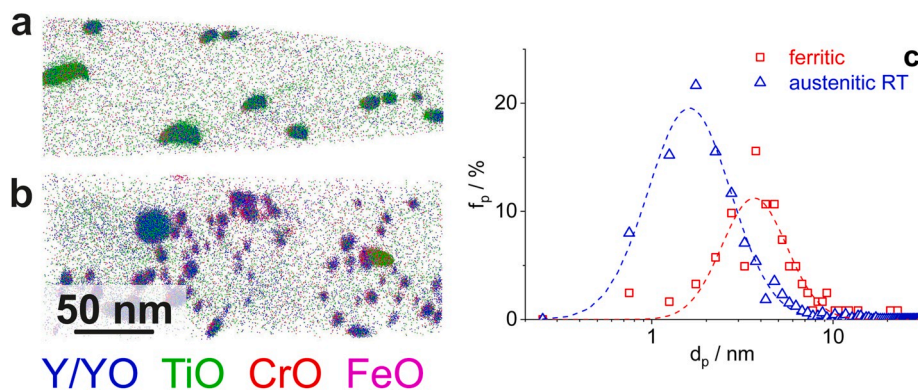


Fig. 4. Reconstruction of atom probe datasets of a) *ferritic* and b) *austenitic RT* in the consolidated state. Positions of the particle ions Y, YO, TiO, CrO and FeO are shown in sections of 30 nm in thickness and 250 nm in length. Other ions are omitted for clarity. c) Size distribution of particles identified by maximum separation method (dashed lines correspond to log-normal distribution fits of the respective datasets).

compression direction during FAST was always chosen to be parallel to the compression direction during compression tests. The experimental yield strength at 0.2% plastic strain was found to be (1851 ± 71) MPa and (916 ± 27) MPa for *ferritic* and *austenitic RT*, respectively (see also Table 3). Errors represent the deviation in at least two compression tests.

In the following, the materials parameters obtained from the multi-scale characterization of the microstructure are used to: (i) calculate the strengthening contributions, (ii) identify differences between the ferritic and austenitic ODS steels, and (iii) assess the modeled yield strength in comparison to the experimental results. All calculated strengthening contributions are summarized in Table 3.

The Peierls stress σ_0 represents the stress required for dislocation motion through a perfect crystal with the periodic Peierls potential. At finite temperature, the stress required to move a dislocation might be reduced due to thermal activation. Theoretical estimates of the Peierls stress (originally by Peierls [62], later corrected by Nabarro [63], and even later with a modified approach by Huntington [64]) typically address the situation without thermal activation and yield a dependence of the stress on the length of the Burgers vector and the width of the dislocation; of which the latter can be expressed in terms of the distance between adjacent slip planes. The available approaches differ significantly (by orders of magnitude) depending on the actual ratio of slip plane distance to Burgers vector length and are strictly restricted to planar dislocation cores which are definitely not the case for screw dislocations in BCC metals and alloys. Furthermore, the estimates are typically complicate to adopt for dislocation dissociation within the slip plane where the dissociated Burgers vectors are not parallel to the resultant Burgers vector which is the case for FCC metals and alloys [65]. Therefore, a theoretical estimate for the current alloys seems vague in the present cases; especially due to the fact that RT and higher temperatures are considered.

In the experimental context and especially when considering strengthening contributions in materials with complex microstructures yielding several different strengthening contributions, the Peierls stress in FCC metals and alloys is typically neglected at finite temperatures. For 0 K, $\sigma_0/G \lesssim 10^{-5}$ [66] is comparably low and thermal activation is sufficient to overcome maxima in the Peierls potential already at rather low temperatures. Therefore, we assume $\sigma_0 \approx 0$ for *austenitic RT* in the present study in accordance with the treatment for FCC metals and alloys in Refs. [67,68]. In contrast, the situation is more complicated for BCC metals and alloys. Here, the microscopic details of slip lead to a generally higher Peierls stress of $10^{-3} < \sigma_0/G \lesssim 10^{-2}$ at 0 K [66]. In conjunction with the thermal activation, a more pronounced temperature dependence of the yield stress is observed [69–72]. For the present case, we assume 100 MPa for the *ferritic* alloy according to Schneibel et al. in Ref. [5]. This is slightly higher than the yield stress of about 70 MPa [73] which was found for Armco iron (extrapolated to infinite grain size) and the yield stress in iron single crystals which was found to be

about 45 MPa [74]. Even though we do not neglect the Peierls stress in the BCC case, its contribution remains still rather small in comparison to the actual yield stress of the ODS alloy and lies in the order of the uncertainty of the experimental yield stress.

Solid solution strengthening σ_{ss} is estimated from the theory of par elastic interaction by the analysis of the lattice parameter dependence on solute concentration, following Eq. (2). Note, that this theory is originally derived for dilute solid solutions which is strictly not valid here [75].

$$\sigma_{ss} = \frac{M \cdot G}{\sqrt{3}} \cdot |\delta|^{3/2} \cdot \sqrt{x} \quad (2)$$

In this equation M is the Taylor factor, which is about 3.1 for all investigated alloys [76]. G is the shear modulus and x the concentration of solute atoms. δ describes the change of the lattice parameter a with varying solute atom concentration:

$$\delta = \frac{d \ln(a)}{dx} \quad (3)$$

Lattice parameters determined from XRD analysis are provided in Table 2 for the investigated alloys. In order to estimate δ , these lattice parameters were compared with the one of pure Fe ($a = 2.867 \text{ \AA}$) [77] and the one of an austenitic ODS steel Fe–16Cr–16Ni–0.4Ti–0.25Y₂O₃ ($a = 3.586 \text{ \AA}$), respectively. Further quantities and their associated values which are necessary for the calculation of strengthening contributions are provided in Table 4. The contribution of solid solution strengthening is found to be 114 MPa for *ferritic* as well as 69 MPa for *austenitic RT*. These are only minor contributions to the total yield strength of both ODS steels.

The contribution of dislocation strengthening σ_{dis} is calculated by means of the classical Taylor equation [78]:

$$\sigma_{dis} = \alpha \cdot M \cdot G \cdot b \cdot \sqrt{\rho_{dis}} \quad (4)$$

The Burger's vectors b are 0.248 nm for *ferritic* [79] and 0.258 nm [79] for *austenitic RT*. α is a constant which is about 0.2 [80] for the investigated alloys. The dislocation densities ρ_{dis} , obtained from the E_{hkl} normalized WH plots, are used. Finally, σ_{dis} equals to 550 MPa for the *ferritic* alloy. As a consequence of the about two orders of magnitude lower dislocation density, σ_{dis} yields only 111 MPa for *austenitic RT*, demonstrating that this strengthening mechanism plays only a minor role in austenitic ODS alloys. This might result from an increased propensity for annihilation of dislocations during the consolidation of the austenitic ODS steel.

The yield strength contribution σ_{HP} as a function of the grain size d_g is expressed by the Hall-Petch relationship [81]:

$$\sigma_{HP} = \frac{k_{HP}}{\sqrt{d_g}} \quad (5)$$

where k_{HP} is the Hall-Petch constant. An overview of available values for k_{HP} in iron-based BCC materials has been provided by Schneibel and Heilmaier [39]. In this work, we use $k_{HP} = 0.6 \text{ MPa m}^{1/2}$ [82] for the *ferritic* alloy. For a broad range of compositions in austenitic steels a smaller Hall-Petch coefficient of $0.3 \text{ MPa m}^{1/2}$ can be found in literature [83,84]. These numbers have to be taken with care, since influences

Table 3

Summary of the experimental yield strength $\sigma_{0.2}$ at RT, the calculated strengthening contributions as well as the rms (σ_{rms}) and linear superposition (σ_{lin}) of these contributions. Strengthening contributions are Peierls stress (σ_0), solid solution strengthening (σ_{ss}), dislocation strengthening (σ_{dis}), Hall-Petch strengthening (σ_{HP}), and Orowan strengthening (σ_{OR}), all values are given in MPa.

	<i>ferritic</i>	<i>austenitic RT</i>
$\sigma_{0.2}$	1851 ± 71	916 ± 27
σ_0	100	0
σ_{ss}	114	69
σ_{dis}	550	111
σ_{HP}	693	423
σ_{OR}	381	811
σ_{rms}	975	924
σ_{lin}	1838	1414

Table 4

Summary of parameters used for the calculation of each strengthening contribution.

Parameter	unit	<i>ferritic</i>	<i>austenitic RT</i>
M	–	3.1	3.1
G	GPa	64 [79]	81 [79]
b	nm	0.248 [79]	0.258 [79]
k_{HP}	MPa m ^{1/2}	0.6 [82]	0.3 [83]
α	–	0.2 [80]	0.2 [80]

from further strengthening contributions (e.g. solid solution strengthening) are not always taken into account in these analyses. In combination with the grain size information obtained from Fig. 3, σ_{HP} is calculated to be 693 MPa for the *ferritic* alloy. Although the grain size of *austenitic RT* is only half of that of the *ferritic* alloy, the Hall-Petch contribution of this alloy is calculated to be only 423 MPa. Hence, it is significantly smaller than for the *ferritic* alloy. This is a direct consequence of the lower Hall-Petch coefficient of the austenite and the $1/\sqrt{d_g}$ dependence of grain size in the Hall-Petch relationship. It has to be highlighted that even though smaller grain sizes can be realized in austenitic ODS steels, it will never be possible to achieve the same Hall-Petch strengthening in comparison to their ferritic counterparts.

To analyze particle strengthening, information about the composition and structure of ODS particles is necessary. Although there is still some controversy on the crystal structure of the nanoclusters in both, ferritic as well as austenitic ODS steels, the existence of cubic $Y_2Ti_2O_7$ is reported in most cases for oxide particles with about 4 nm in size [27,35,36,85]. Predominantly, a (semi-)coherent cube-on-cube orientation relation between particles and matrix is found, from which it can be assumed that dislocations cannot penetrate the nanoclusters without destroying the crystal structure of the clusters. Furthermore, larger particles (>10 nm) are reported to be incoherent [35], while APT analysis of the smallest nanoclusters (<2 nm) revealed a non-stoichiometric composition and a lack of a well-defined crystal structure [35,86]. Hence, it can be expected that dislocations could possibly cut only the smallest particles, but a majority of oxide particles has to be overcome by the Orowan mechanism. Therefore, we adopt the Orowan relation for this strengthening contribution at RT as [43]:

$$\sigma_{OR} = \frac{M \cdot G \cdot b}{d_p} \sqrt{\frac{6 \cdot f_p}{\pi}} \quad (6)$$

In this equation d_p represents the size and f_p the volume fraction of nanoclusters. f_p can be calculated by means of the nanocluster density ρ_p . Nevertheless, it has to be mentioned that the calculation related to the Orowan mechanism rather overestimates the particle strengthening contribution. Both, d_p and ρ_p are obtained from atom probe data:

$$f_p = \frac{4}{3} \cdot \pi \cdot \left(\frac{d_p}{2}\right)^3 \cdot \rho_p \quad (7)$$

Combining (6) and (7), thus, yields:

$$\sigma_{OR} = M \cdot G \cdot b \cdot \sqrt{d_p \cdot \rho_p} \quad (8)$$

Using data presented in Tables 2 and 4, the Orowan contributions are calculated to be 381 MPa and 811 MPa for the *ferritic* alloy and *austenitic RT*, respectively. The higher Orowan contribution of *austenitic RT* essentially results from the smaller nanocluster size and the higher particle density determined for that alloy.

Taking all calculated strengthening contributions into account, the lower and upper limit of the yield strength is calculated following Eq. (1). The lower limit given by the rms of the contributions is 975 MPa for the *ferritic* alloy and 924 MPa for *austenitic RT*. The linear superposition of the strengthening contributions represents the upper limit of the yield strength, which is 1838 and 1414 MPa for *ferritic* and *austenitic RT*, respectively.

Fig. 5 visualizes the superposition of each strengthening contribution σ_i and compares the calculated yield strength limits to the experimental ones (grey bars). The lower limit provided by the root mean square is shown as cyan bars. Strengthening contributions to the upper limit by linear superposition are color-coded as follows: Peierls stress (purple), solid solution strengthening (blue), dislocation strengthening (green), Hall-Petch strengthening (orange) and Orowan strengthening (red). In case of the *ferritic* alloy experimental yield strength and the linear superposition of strengthening contributions are in good agreement while for *austenitic RT* the rms seems to better reproduce the experimental

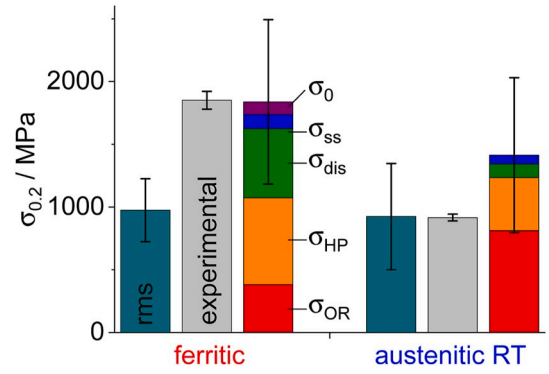


Fig. 5. Calculated strength in comparison to the experimentally (grey bars) determined yield strength (RT, initial strain rate $\dot{\epsilon} = 10^{-4} \text{ s}^{-1}$). The lower limit represents the rms concept (cyan). The linear superposition to the upper limit of the strengthening contributions is color-coded as follows: Orowan strengthening (red), Hall-Petch strengthening (orange), dislocation strengthening (green), solid solution strengthening (blue) and Peierls stress (purple). (For interpretation of the references to color in this figure legend, the reader is referred to the Web version of this article.)

result. The yield strength of the investigated materials depends on multiple strengthening mechanisms varying in strength and number density [44]. Possible interactions between the aforementioned strengthening mechanisms are not further investigated in this work. Besides the discussion about how to superimpose the various strengthening contributions, the uncertainties (i) in experimental evaluation of relevant parameters or (ii) published parameters which control these strengthening mechanisms have to be assessed. The detailed discussion of the uncertainties in chapter 3.4 leads to the definition of the error bars for the superpositions given in Fig. 5.

3.4. Assessment of uncertainties

Uncertainties of the various strengthening contributions are visualized in Fig. 6. For a critical assessment of the uncertainties due to deviations in the published parameters, minimum and maximum values are assumed in the following. The uncertainties of experimentally determined parameters result either from the determination process of these parameters (namely for dislocation and particle density) or from a distribution of the considered parameter within the microstructure under investigation (namely grain sizes and particle sizes). In this work, the standard deviation is used to rationalize these uncertainties. The uncertainty of each strengthening contribution is calculated using the law of error propagation. Therefore, only uncertainties of experimental parameters are taken into account, which are supposed to be dominating over uncertainties from parameters taken from literature.

Fig. 6a visualizes the possible range of dislocation strengthening for both investigated ODS steels, by showing colored regions (red for *ferritic* and blue for *austenitic RT*). Following Eq. (4), dislocation strengthening is determined by the constant α and the experimentally obtained dislocation density ρ_{dis} . Upper and lower limits are calculated with $\alpha = 0.15$ and 0.25 [80], respectively, for the ferritic and austenitic alloy. The uncertainty of dislocation density obtained from XRD analysis is visualized by the width of the colored regions representing the standard deviation of ρ_{dis} . The uncertainty of dislocation strengthening $\Delta\sigma_{dis}$, resulting from the dislocation density is 176 and 13 MPa for the *ferritic* alloy and *austenitic RT*, respectively (Table 5).

The Hall-Petch strengthening depending on the Hall-Petch coefficient k_{HP} and the grain size d_g is visualized in Fig. 6b. The uncertainties due to variation of the Hall-Petch constants are represented by the upper and lower limit of the colored regions, which are set to $\pm 0.1 \text{ MPa m}^{1/2}$ of the initial k_{HP} value of the *ferritic* alloy [39] as well as $\pm 0.05 \text{ MPa m}^{1/2}$ of *austenitic RT* [87]. Grain size as determined from EBSD mappings is

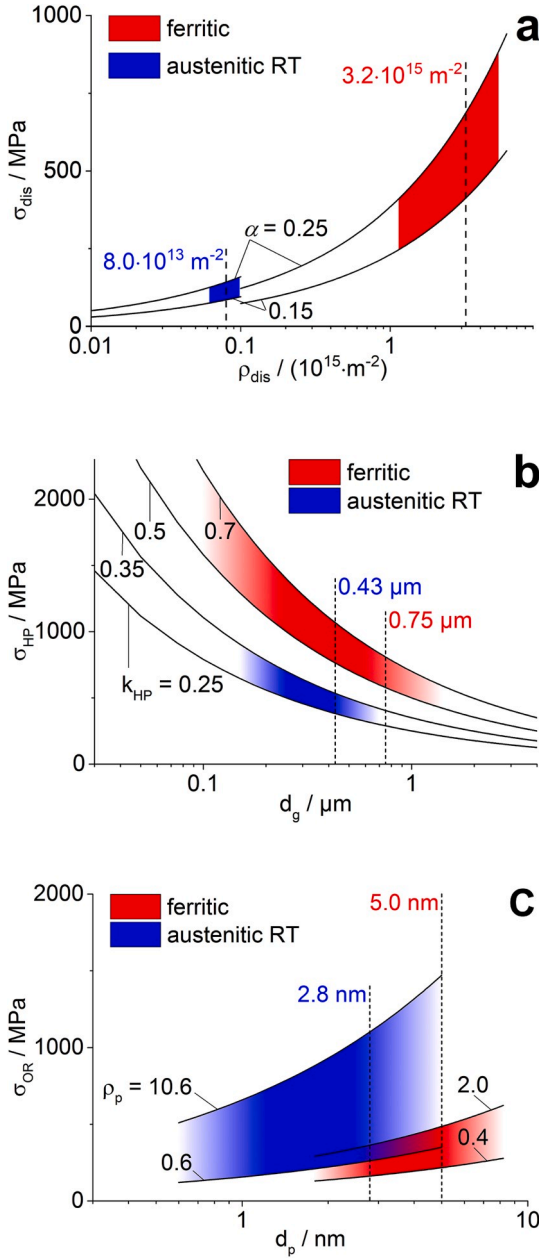


Fig. 6. Visualization of uncertainties, occurring in the calculation of the most relevant strengthening contribution at RT, for: a) dislocation strengthening, b) Hall-Petch strengthening (k_{HP} for upper and lower bounds given in $MPa m^{1/2}$) and c) Orowan strengthening (ρ_p for upper and lower bounds given in $10^{22} m^{-3}$). Color fade-outs illustrate uncertainties resulting from the size distribution of grains and particles. Given values represent mean experimental results from materials characterization. (For interpretation of the references to color in this figure legend, the reader is referred to the Web version of this article.)

Table 5

Summary of the uncertainties resulting from experimentally determined parameters for the calculation of strengthening contributions, all values are given in MPa.

Alloy	$\Delta\sigma_{dis}$	$\Delta\sigma_{HP}$	$\Delta\sigma_{OR}$	$\Delta\sigma_{tot}^{rms}$	$\Delta\sigma_{tot}^{linear}$
ferritic	176	305	174	251	655
austenitic RT	13	130	473	423	616

indicated for the investigated alloys. The width of the colored and faded regions represents the grain size distribution (see Fig. 3c). The uncertainty of Hall-Petch strengthening $\Delta\sigma_{HP}$ due to grain size deviation is 305 and 130 MPa for the ferritic alloy and austenitic RT, respectively (Table 5) which is much larger than the influence of deviations in k_{HP} for both alloys.

Orowan strengthening depends on two experimentally determined parameters, namely size and density of nanoclusters. The resulting uncertainty of this strengthening contribution is shown in Fig. 6c. Upper and lower limits of the colored regions are determined from the standard deviation of the particle density. The width of the colored areas represents the deviation in particle size. The color fade-out indicates that the uncertainties result from the material-specific particle size distribution depicted in Fig. 4c. The uncertainty of Orowan strengthening $\Delta\sigma_{OR}$ is calculated to be 174 and 473 MPa for the ferritic alloy and austenitic RT, respectively (Table 5).

Table 5 shows that the ferritic alloy has larger uncertainties regarding dislocation and Hall-Petch strengthening. This alloy has the larger contributions of these strengthening mechanisms, too. In case of Orowan strengthening, the uncertainties of both alloys are comparably high, as a consequence of being derived from two experimentally determined parameters. Nevertheless, the uncertainty for austenitic RT is considerably higher as this alloy has the larger Orowan contribution.

The total uncertainties $\Delta\sigma_{tot}$ for rms and linear superposition are calculated following the error propagation and are given in Table 5. $\Delta\sigma_{tot}$ provides a measure for the experimentally accessible accuracy of the yield strength calculation and is in the range of several hundred MPa. It is visualized by the black error bars in the bar chart of the rms and linear superposition in Fig. 5. It can be assumed from Fig. 6 that the uncertainties resulting from parameters based on literature (not included in this discussion) are smaller than the experimental uncertainties. Hence, uncertainties from the determination process of microstructural parameters (e.g. dislocation density or particle density) as well as from the distribution of microstructural features (e.g. grain size or particle size) always lead to an interval of modeled yield strengths. This cannot simply be neglected as it is often done when strengthening contributions are calculated [88]. In other words, it is not possible to precisely calculate the yield strength and one should consider the applied models valid if the experimental yield strength falls within the uncertainty range.

Furthermore, it remains unclear if all strengthening mechanisms are fully operative. As introduced above, particle cutting could possibly occur for the smallest clusters, for which only lower stresses might be needed. This would also explain the overestimation of the Orowan strengthening, as reported by Schneibel et al. [5].

3.5. Modeling of the temperature dependent compressive strength

Fig. 7 summarizes the compressive yield strength of both investigated alloys at temperatures between RT and 800 °C, visualized by the open symbols. In the entire temperature range, the ferritic alloy shows higher yield strength than austenitic RT. In the following, the temperature range up to about 500 °C is referred to as low temperature (LT). In the LT range, a slight continuous decrease in yield strength is observed which is largely governed by the temperature dependence of the shear modulus. Above, at the sudden drop of yield strength at about 500 °C, high temperature (HT) deformation mechanisms set in. This is in line with the concept of homologous temperature since melting temperatures are about 1800 K (≈ 1520 °C) [89] for ferritic and 1700 K (≈ 1420 °C) [90] for austenitic RT; $0.4 \cdot T_m$ would thus correspond to temperatures of 720 K (≈ 450 °C) for ferritic and 680 K (≈ 410 °C) for austenitic RT. At 600 °C, yield strength has dropped already to 300 MPa for the ferritic alloy and to 100 MPa for austenitic RT. Further increase in temperature results in an only slight further decrease of yield strength.

In order to describe the temperature dependence of the yield strength, the simple linear superposition of strengthening contributions

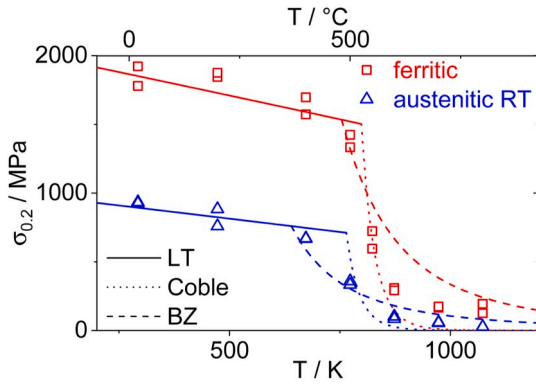


Fig. 7. Results of temperature dependent compression tests. All alloys reveal the common modulus dependent decrease in strength in the low temperature (LT) range. Sudden drop of strength at about 500 °C is observed, defining the onset of the high temperature (HT) deformation range. Lines represent model-based description of the strength. Linear superposition of strengthening contributions was assumed in the LT range (solid lines). HT strength is described by creep models of Coble (dotted lines) as well as Blum and Zeng (BZ, dashed lines), respectively.

is combined with the creep models by Coble [51] as well as by Blum and Zeng (BZ) [52,53], respectively. In the case of *austenitic RT* the model-based summation of strengthening contributions was found to be higher in comparison to experimental yield strength data due to reasons explained above. Hence, a linear scaling factor of 0.6 is applied to the calculated yield strength to fit it to experimental data. Note that after applying the scaling factor, the calculated yield strength is still higher than following the rms concept of superposition, which gives the lower limit of strength. The LT fit allows the determination of the transition temperature to creep-based deformation mechanisms later on. Furthermore, the slightly decreasing strength in the LT range is depicted by the temperature dependent decrease in shear modulus for which $T_m/G(300\text{ K}) \cdot dG/dT = -0.81$ and -0.85 for *ferritic* and *austenitic RT* is found in literature [79], respectively. Additionally, Hall-Petch strengthening follows Eq. (9) from Ref. [91], in which $G(T)$ is the shear modulus at a given temperature and $G(RT)$ is the shear modulus at RT:

$$\sigma_{HP}(T) = \sqrt{\frac{G(T)}{G(RT)}} \cdot \frac{k_{HP}}{\sqrt{d_g}} \quad (9)$$

The strength at HT is significantly altered by creep deformation. Therefore, a stress-strain rate dependence is observed. As introduced earlier, one possible model describing the drop of yield strength, is the grain boundary diffusion-based model by Coble [51] which is presented next in the (non-conventional) form of stress dependent on strain rate:

$$\sigma_C = \frac{k_B \cdot T \cdot d_g^3}{47 \cdot \Omega \cdot \delta_{gb} \cdot D_{gb0}} \cdot \exp\left(\frac{Q_{gb}}{8 \cdot N_A \cdot k_B \cdot T}\right) \cdot \dot{\epsilon} \quad (10)$$

Creep stress σ_C depends on the applied temperature T , the strain rate $\dot{\epsilon}$ and the grain size d_g . Further, k_B is the Boltzmann constant ($k_B = 1.381 \cdot 10^{-23}$ J/K) and N_A the Avogadro constant ($= 6.022 \cdot 10^{23}$ mol $^{-1}$). Materials constants are the atomic volume Ω , the grain boundary width δ_{gb} and the scaling factor for grain boundary diffusion D_{gb0} as well as the activation energy for grain boundary diffusion Q_{gb} . Quantitative numbers of these parameters which are used for this work are given in Table 6. Following Eq. (10) possible parameters to fit the Coble model to experimental data are the coefficient $\delta_{gb} \cdot D_{gb0}$ and the activation energy Q_{gb} . Since variations of $\delta_{gb} \cdot D_{gb0}$ and Q_{gb} are acting in the same way, only Q_{gb} , for which comparative values can be found in literature is used for the fitting procedure.

The dislocation-based creep model following BZ is based on the assumption that creep is controlled by a steady-state process of annihilation and generation of dislocations at grain boundaries [52]. Schneibel

Table 6

Summary of parameters used for the calculation of strength following the Coble and the BZ model, respectively.

Parameter	unit	Ferritic	austenitic RT
$\dot{\epsilon}$	s $^{-1}$	10^{-4}	10^{-4}
ν	–	0.2 [39]	0.2 [39]
Ω	\AA^3	0.00118 [79]	0.00121 [79]
$\delta_{gb} \cdot D_{gb0}$	10^{-12} m 2 /s	1.1 [79]	0.2 [79]
Q_{gb}	kJ/mol	174 [79]	167 [79]
α (in Ref. [53])	–	0.2 [80]	–
c (in Ref. [53])	–	0.5 [53]	–
k_{BZ}	–	0.45	0.45

et al. [5,39] obtained reasonable results using the BZ model to describe the drop in yield strength of ferritic ODS steels. The creep stress σ_{BZ} based on this model is given by Ref. [52,53]:

$$\sigma_{BZ} = k_{BZ} \cdot G \left(\frac{\pi \cdot (1 - \nu) \cdot M^9}{1, 2^4} \right)^{\frac{1}{9}} \cdot \left(\frac{k_B \cdot T}{G \cdot \delta_{gb} \cdot D_{gb0}} \cdot \dot{\epsilon} \right)^{\frac{1}{9}} \cdot \exp\left(\frac{Q_{gb}}{8 \cdot N_A \cdot k_B \cdot T}\right) \cdot \left(\frac{d_g}{b}\right)^{-\frac{1}{9}} \quad (11)$$

The shear modulus G , Poisson's ratio ν , Taylor factor M and the length of the Burgers vector b are materials constants. Obviously, quite different dependencies of creep stress on temperature, strain rate and grain size are noted in comparison to the Coble model which, however, allow for an unambiguous differentiation between the two proposed models when applied to experimental data.

Compared to the original BZ equation from Ref. [52], several simplifications were made: Assuming that the grain boundary thickness is in the order of b , the quotient δ_{gb}/b in Eq. (19) of Ref. [52] is set to unity. Following Schneibel and Heilmaier [39], ξ in Eq. (6) of Ref. [52] can be set to zero leading to $f(\xi) = 1$ in Eq. (18) of Ref. [52], which means that no spontaneous annihilation of dislocation occurs in the grain boundary. Additionally, the parameters α and c in Refs. [53] are summarized in this work as constant k_{BZ} , which should lie in the range between 0.2 and 5 [39,53]. With $\alpha = 0.2$ [80] and $c = 0.5$ (lowest value for c taken in Ref. [53]) $k_{BZ} = 0.45$ is obtained. Again, Q_{gb} is used to fit the data, while $\delta_{gb} \cdot D_{gb0}$ remains constant for the reasons explained above.

When literature data is used, the drop in strength is predicted for lower temperatures compared to experimental results in the Coble model as well as the BZ model. Increasing activation energies result in a shift of the curves to higher temperatures in both models. The results from fitting Q_{gb} are represented by the solid and dashed lines in Fig. 7 and optimized parameters are summarized in Table 7. It is obvious from Fig. 7, that the Coble model is not able to properly describe the drop in yield strength. Although the obtained activation energies of both investigated alloys are in the same range compared to the initial numbers (Table 6), the drop in strength is too strong and strength approaches zero too quickly. Calculations following the BZ model give more appropriate results. Obtained Q_{gb} values (Table 7) are higher than given in literature for the self-diffusion of Fe in grain boundaries. Higher apparent activation energies (up to 300 kJ/mol) compared to the reference materials without oxide particles have already been reported for ODS steels [92,93]. Possible mechanisms leading to increased activation energies in ODS materials are strong dislocation-oxide particle interaction [94–96] and a slowed down diffusion by the nano-sized

Table 7

Optimized parameters for the description of the temperature dependent yield strength on the basis of presented strengthening models in the LT as well as the HT range, all values are given in kJ/mol.

alloy	Q_{gb} for Coble	Q_{gb} for BZ
ferritic	188	325
austenitic RT	175	223

particles, being located on grain boundaries [4]. Nevertheless, dislocation-based creep is assumed from this analysis to be the dominant creep mechanism in the HT range.

4. Summary

The main focus of this work was on the model-based description of the strength of ferritic and austenitic ODS steels in the temperature range from RT to 800 °C. Therefore, ferritic and austenitic ODS steels were manufactured by mechanical alloying and subsequent consolidation. Characterization of microstructure and of mechanical properties by means of compression tests have been conducted. The outstanding results from this work are summarized as follows:

- Austenitic ODS steels with sub-micron grain size and nanometer-sized oxide particles similar to ferritic ODS steels can be produced by mechanical alloying and subsequent consolidation by field assisted sintering technique. Starting from elemental powders is preferred due to a more homogenous distribution of particles in the material and absence of large grain regions compared to austenitic ODS steels from ductile, pre-alloyed powder. Formation of a homogenous single-phase, austenitic microstructure is obtained during the consolidation process.
- Multiscale characterization of the microstructure by XRD, EBSD and APT allowed the calculation and critical assessment of strengthening contributions. From that, Hall-Petch and dislocation strengthening are identified as crucial strengthening mechanisms explaining the superior RT strength of ferritic ODS steels in comparison to their austenitic counterparts.
- Inferior dislocation strengthening is explained by intense recovery and/or recrystallization occurring in austenitic ODS steels during consolidation. An increased yield strength is expected for austenitic ODS steels with modified composition to obtain lower stacking fault energies and, hence, reduced recovery during consolidation.
- The linear superposition of calculated strengthening mechanisms tends to overestimate the experimental results. Nevertheless, if the interaction of the strengthening mechanisms and the uncertainties of determined parameters are taken into account, the calculated strength satisfactorily fits experimental results. It becomes apparent that a critical discussion of experimental data is necessary if strengthening theories are applied to describe the strength of complex materials.
- From fitting the temperature dependent strength using the Coble and the BZ model, it can be concluded that the creep-controlled drop of strength above 400–500 °C in ODS steels can be explained by the BZ model more appropriately and hence, dislocation annihilation and generation of dislocations at grain boundaries might dominate deformation at high temperatures.

Prime novelty statement

We confirm that this manuscript has not been published previously by any of the authors and is not under consideration for publication in another journal.

Declaration of competing interest

The authors declare that they have no known competing financial interests or personal relationships that could have appeared to influence the work reported in this paper.

CRediT authorship contribution statement

S. Seils: Conceptualization, Methodology, Investigation, Writing - original draft, Visualization. **A. Kauffmann:** Conceptualization, Methodology, Investigation, Writing - original draft, Visualization,

Supervision. **F. Hinrichs:** Methodology, Investigation, Writing - review & editing. **D. Schliephake:** Methodology, Investigation, Writing - review & editing. **T. Boll:** Methodology, Investigation, Writing - review & editing. **M. Heilmaier:** Resources, Writing - review & editing, Supervision, Resources, Funding acquisition.

Acknowledgements

The authors acknowledge the financial support through DFG contract no. HE1872/23–1. This work has also received funding from the topic “Materials Research for the Future Energy Supply” within the framework of the Helmholtz Association. This work was partly carried out with the support of the Karlsruhe Nano Micro Facility (KNMF, www.knmf.kit.edu), a Helmholtz Research Infrastructure at Karlsruhe Institute of Technology (KIT, www.kit.edu). We acknowledge G. Schell at IAM-KWT at KIT for the support in sample consolidation as well as IAM-AWP at KIT for the chemical analysis by ICP-OES. S. Laube, L. Wengenmayer and C. Kurpiers are acknowledged for their support in sample preparation and J. N. Wagner for fruitful discussions. AK thanks the Carl Zeiss Foundation for financial support via a Postdoctoral Grant.

References

- [1] S. Ukai, M. Harada, H. Okada, M. Inoue, S. Nomura, S. Shikakura, K. Asabe, T. Nishida, M. Fujiwara, Alloying design of oxide dispersion strengthened ferritic steel for long life FBRs core materials, *J. Nucl. Mater.* 204 (1993) 65–73, [https://doi.org/10.1016/0022-3115\(93\)90200-1](https://doi.org/10.1016/0022-3115(93)90200-1).
- [2] S. Ukai, M. Harada, H. Okada, M. Inoue, S. Nomura, S. Shikakura, T. Nishida, M. Fujiwara, K. Asabe, Tube manufacturing and mechanical properties of oxide dispersion strengthened ferritic steel, *J. Nucl. Mater.* 204 (1993) 74–80, [https://doi.org/10.1016/0022-3115\(93\)90201-9](https://doi.org/10.1016/0022-3115(93)90201-9).
- [3] J. Ohta, T. Ohmura, K. Kako, M. Tokiwa, T. Suzuki, Hardness of 12Cr8Mo ferritic steels irradiated by Ni ions, *J. Nucl. Mater.* 225 (1995) 187–191, [https://doi.org/10.1016/0022-3115\(95\)00016-X](https://doi.org/10.1016/0022-3115(95)00016-X).
- [4] J.H. Schneibel, C.T. Liu, M.K. Miller, M.J. Mills, P. Sarosi, M. Heilmaier, D. Sturm, Ultrafine-grained nanocluster-strengthened alloys with unusually high creep strength, *Scripta Mater.* 61 (2009) 793–796, <https://doi.org/10.1016/j.scriptamat.2009.06.034>.
- [5] J.H. Schneibel, M. Heilmaier, W. Blum, G. Hasemann, T. Shanmugasundaram, Temperature dependence of the strength of fine- and ultrafine-grained materials, *Acta Mater.* 59 (2011) 1300–1308, <https://doi.org/10.1016/j.actamat.2010.10.062>.
- [6] S. Ukai, M. Fujiwara, Perspective of ODS alloys application in nuclear environments, *J. Nucl. Mater.* 307 (2002) 749–757, [https://doi.org/10.1016/S0022-3115\(02\)01043-7](https://doi.org/10.1016/S0022-3115(02)01043-7).
- [7] M.K. Miller, E.A. Kenik, K.F. Russell, L. Heatherly, D.T. Hoelzer, P.J. Maziasz, Atom probe tomography of nanoscale particles in ODS ferritic alloys, *Mater. Sci. Eng.* 353 (2003) 140–145, [https://doi.org/10.1016/S0921-5093\(02\)00680-9](https://doi.org/10.1016/S0921-5093(02)00680-9).
- [8] C.A. Williams, E.A. Marquis, A. Cerezo, G.D.W. Smith, Nanoscale characterisation of ODS-Eurofer 97 steel: an atom-probe tomography study, *J. Nucl. Mater.* 400 (2010) 37–45, <https://doi.org/10.1016/j.jnucmat.2010.02.007>.
- [9] M.J. Alinger, G.R. Odette, D.T. Hoelzer, The development and stability of Y–Ti–O nanoclusters in mechanically alloyed Fe–Cr based ferritic alloys, *J. Nucl. Mater.* 329 (2004) 382–386, <https://doi.org/10.1016/j.jnucmat.2004.04.042>.
- [10] A. Hirata, T. Fujita, Y.R. Wen, J.H. Schneibel, C.T. Liu, M.W. Chen, Atomic structure of nanoclusters in oxide-dispersion strengthened steels, *Nat. Mater.* 10 (2011) 922–926, <https://doi.org/10.1038/nmat3150>.
- [11] J.S. Benjamin, Dispersion strengthened superalloys by mechanical alloying, *Metallurgical Transactions* 1 (1970) 2943–2951, <https://doi.org/10.1007/BF03037835>.
- [12] U. Grundmann, M. Heilmaier, U. Martin, H. Oettel, L. Schultz, Oxide dispersion-strengthened silver: manufacturing and properties, *Z. Metallkd.* 94 (2003) 587–592, <https://doi.org/10.3139/146.030587>.
- [13] U. Martin, M. Heilmaier, Novel dispersion strengthened metals by mechanical alloying, *Adv. Eng. Mater.* 6 (2004) 515–520, <https://doi.org/10.1002/adem.200400410>.
- [14] M. Heilmaier, H. Saage, J. Eckert, Formation of ODS L1₂–(Al,Cr)₃Ti by mechanical alloying, *Mater. Sci. Eng.* 239–240 (1997) 652–657, [https://doi.org/10.1016/S0921-5093\(97\)00644-8](https://doi.org/10.1016/S0921-5093(97)00644-8).
- [15] C. Heintze, M. Hernández-Mayoral, A. Ulbricht, F. Bergner, A. Shariq, T. Weissgärber, H. Frielinghaus, Nanoscale characterization of ODS Fe–9%Cr model alloys compacted by spark plasma sintering, *J. Nucl. Mater.* 428 (2012) 139–146, <https://doi.org/10.1016/j.jnucmat.2011.08.053>.
- [16] K. Oka, S. Ohnuki, S. Yamashita, N. Akasaka, S. Ohtsuka, H. Tanigawa, Structure of nano-size oxides in ODS steels and its stability under electron irradiation, *Mater. Trans.* 48 (2007) 2563–2566, <https://doi.org/10.2320/matertrans.MD200715>.
- [17] A.W. Bowen, G.M. Leak, Solute diffusion in alpha- and gamma-iron, *Metallurgical Transactions* 1 (1970) 1695–1700, <https://doi.org/10.1007/BF02642019>.

- [18] Y. Peng, L. Yu, Y. Liu, Z. Ma, H. Li, C. Liu, J. Wu, Microstructures and tensile properties of an austenitic ODS heat resistance steel, *Mater. Sci. Eng.* 767 (2019), <https://doi.org/10.1016/j.msea.2019.138419>, 138419.
- [19] Y. Miao, K. Mo, Z. Zhou, X. Liu, K.-C. Lan, G. Zhang, M.K. Miller, K.A. Powers, J. Almer, J.F. Stubbins, In situ synchrotron tensile investigations on the phase responses within an oxide dispersion-strengthened (ODS) 304 steel, *Mater. Sci. Eng.* 625 (2015) 146–152, <https://doi.org/10.1016/j.msea.2014.12.017>.
- [20] M. Wang, Z. Zhou, H. Sun, H. Hu, S. Li, Microstructural observation and tensile properties of ODS-304 austenitic steel, *Mater. Sci. Eng.* 559 (2013) 287–292, <https://doi.org/10.1016/j.msea.2012.08.099>.
- [21] Z. Zhou, S. Yang, W. Chen, L. Liao, Y. Xu, Processing and characterization of a hiped oxide dispersion strengthened austenitic steel, *J. Nucl. Mater.* 428 (2012) 31–34, <https://doi.org/10.1016/j.jnucmat.2011.08.027>.
- [22] Y. Xu, Z. Zhou, M. Li, P. He, Fabrication and characterization of ODS austenitic steels, *J. Nucl. Mater.* 417 (2011) 283–285, <https://doi.org/10.1016/j.jnucmat.2010.12.155>.
- [23] P. Susila, D. Sturm, M. Heilmaier, B.S. Murty, V.S. Sarma, Microstructural studies on nanocrystalline oxide dispersion strengthened austenitic (Fe-18Cr-8Ni-2W-0.25Y2O3) alloy synthesized by high energy ball milling and vacuum hot pressing, *J. Mater. Sci.* 45 (2010) 4858–4865, <https://doi.org/10.1007/s10853-010-4264-3>.
- [24] Z. Zhou, S. Sun, L. Zou, Y. Schneider, S. Schmauder, M. Wang, Enhanced strength and high temperature resistance of 25Cr20Ni ODS austenitic alloy through thermo-mechanical treatment and addition of Mo, *Fusion Eng. Des.* 138 (2019) 175–182, <https://doi.org/10.1016/j.fusengdes.2018.11.020>.
- [25] Y. Miao, K. Mo, Z. Zhou, X. Liu, K.-C. Lan, G. Zhang, J.-S. Park, J. Almer, J. F. Stubbins, Load-partitioning in an oxide dispersion-strengthened 310 steel at elevated temperatures, *Mater. Des.* 111 (2016) 622–630, <https://doi.org/10.1016/j.matdes.2016.09.015>.
- [26] M. Wang, Z. Zhou, H. Sun, H. Hu, S. Li, Effects of plastic deformations on microstructure and mechanical properties of ODS-310 austenitic steel, *J. Nucl. Mater.* 430 (2012) 259–263, <https://doi.org/10.1016/j.jnucmat.2012.07.014>.
- [27] J.R.O. Leo, S. Pirfo Barroso, M.E. Fitzpatrick, M. Wang, Z. Zhou, Microstructure, tensile and creep properties of an austenitic ODS 316L steel, *Mater. Sci. Eng.* 749 (2019) 158–165, <https://doi.org/10.1016/j.msea.2019.02.014>.
- [28] T. Gräning, M. Klimenkov, M. Rieth, C. Heintze, A. Möslang, Long-term stability of the microstructure of austenitic ODS steel rods produced with a carbon-containing process control agent, *J. Nucl. Mater.* 523 (2019) 111–120, <https://doi.org/10.1016/j.jnucmat.2019.05.060>.
- [29] C. Dai, L. Kurmanaeva, C. Schade, E. Lavernia, D. Apelian, Microstructure and mechanical behavior of ODS stainless steel fabricated using cryomilling, *Metall. Mater. Trans.* 50 (2019) 5767–5781, <https://doi.org/10.1007/s11661-019-05479-4>.
- [30] T. Gräning, M. Rieth, J. Hoffmann, A. Möslang, Production, microstructure and mechanical properties of two different austenitic ODS steels, *J. Nucl. Mater.* 487 (2017) 348–361, <https://doi.org/10.1016/j.jnucmat.2017.02.034>.
- [31] X. Mao, S.H. Kang, T.K. Kim, S.C. Kim, K.H. Oh, J. Jang, Microstructure and mechanical properties of ultrafine-grained austenitic oxide dispersion strengthened steel, *Metall. Mater. Trans.* 47 (2016) 5334–5343, <https://doi.org/10.1007/s11661-016-3570-z>.
- [32] R. Gao, W. Ge, S. Miao, T. Zhang, X. Wang, Q. Fang, Hot rolling and annealing effects on the microstructure and mechanical properties of ODS austenitic steel fabricated by electron beam selective melting, *Front. Mater. Sci.* 10 (2016) 73–79, <https://doi.org/10.1007/s11706-016-0327-y>.
- [33] Y. Miao, K. Mo, Z. Zhou, X. Liu, K.-C. Lan, G. Zhang, M.K. Miller, K.A. Powers, Z.-G. Mei, J.-S. Park, J. Almer, J.F. Stubbins, On the microstructure and strengthening mechanism in oxide dispersion-strengthened 316 steel: a coordinated electron microscopy, atom probe tomography and in situ synchrotron tensile investigation, *Mater. Sci. Eng.* 639 (2015) 585–596, <https://doi.org/10.1016/j.msea.2015.05.064>.
- [34] T.-K. Kim, C.-S. Bae, D.-H. Kim, J.-S. Jang, S.-H. Kim, C.-B. Lee, D.-H. Hahn, Microstructural observation and tensile isotropy of an austenitic ODS steel, *Nuclear Engineering and Technology* 40 (2008) 305–310, <https://doi.org/10.5516/NET.2008.40.4.305>.
- [35] Y. Miao, K. Mo, Z. Zhou, X. Liu, K.-C. Lan, G. Zhang, M.K. Miller, K.A. Powers, J. F. Stubbins, Size-dependent characteristics of ultra-fine oxygen-enriched nanoparticles in austenitic steels, *J. Nucl. Mater.* 480 (2016) 195–201, <https://doi.org/10.1016/j.jnucmat.2016.08.014>.
- [36] T. Gräning, M. Rieth, J. Hoffmann, S. Seils, P.D. Edmondson, A. Möslang, Microstructural investigation of an extruded austenitic oxide dispersion strengthened steel containing a carbon-containing process control agent, *J. Nucl. Mater.* 516 (2019) 335–346, <https://doi.org/10.1016/j.jnucmat.2019.01.048>.
- [37] D.T. Hoelzer, J. Bentley, M.A. Sokolov, M.K. Miller, G.R. Odette, M.J. Alinger, Influence of particle dispersions on the high-temperature strength of ferritic alloys, *J. Nucl. Mater.* 367–370 (2007) 166–172, <https://doi.org/10.1016/j.jnucmat.2007.03.151>.
- [38] M.K. Miller, D.T. Hoelzer, E.A. Kenik, K.F. Russell, Stability of ferritic MA/ODS alloys at high temperatures, *Intermetallics* 13 (2005) 387–392, <https://doi.org/10.1016/j.intermet.2004.07.036>.
- [39] J.H. Schneibel, M. Heilmaier, Hall-petch breakdown at elevated temperatures, *Mater. Trans.* 55 (2014) 44–51, <https://doi.org/10.2320/matertrans.MA201309>.
- [40] D.T. Hoelzer, K.A. Unocic, M.A. Sokolov, T.S. Byun, Influence of processing on the microstructure and mechanical properties of 14YWT, *J. Nucl. Mater.* 471 (2016) 251–265, <https://doi.org/10.1016/j.jnucmat.2015.12.011>.
- [41] J.H. Kim, T.S. Byun, D.T. Hoelzer, C.H. Park, J.T. Yeom, J.K. Hong, Temperature dependence of strengthening mechanisms in the nanostructured ferritic alloy 14YWT: Part II—mechanistic models and predictions, *Mater. Sci. Eng.* 559 (2013) 111–118, <https://doi.org/10.1016/j.msea.2012.08.041>.
- [42] A. Chauhan, F. Bergner, A. Etienne, J. Aktaa, Y. de Carlan, C. Heintze, D. Litvinov, M. Hernandez-Mayoral, E. Onorbe, B. Radigue, A. Ulbricht, Microstructure characterization and strengthening mechanisms of oxide dispersion strengthened (ODS) Fe-9%Cr and Fe-14%Cr extruded bars, *J. Nucl. Mater.* 495 (2017) 6–19, <https://doi.org/10.1016/j.jnucmat.2017.07.060>.
- [43] P.M. Hazzledine, Direct versus indirect dispersion hardening, *Scripta Metall. Mater.* 26 (1992) 57–58, [https://doi.org/10.1016/0956-716X\(92\)90368-O](https://doi.org/10.1016/0956-716X(92)90368-O).
- [44] U.F. Kocks, A.S. Argon, M.F. Ashby, Thermodynamics and kinetics of slip, *Prog. Mater. Sci.* 19 (1975) 1–291.
- [45] A.J. Ardell, Precipitation hardening, *Metallurgical Transactions A* 16 (1985) 2131–2165, <https://doi.org/10.1007/BF02670416>.
- [46] T.J. Koppelaar, D. Kuhlmann-Wilsdorf, The effect of prestressing on the strength of neutron-irradiated copper single crystals, *Appl. Phys. Lett.* 4 (1964) 59–61, <https://doi.org/10.1063/1.1753962>.
- [47] E. Nembach, Synergetic effects in the superposition of strengthening mechanisms, *Acta Metall. Mater.* 40 (1992) 3325–3330, [https://doi.org/10.1016/0956-7151\(92\)90045-G](https://doi.org/10.1016/0956-7151(92)90045-G).
- [48] P. Miao, G.R. Odette, T. Yamamoto, M. Alinger, D. Klingensmith, Thermal stability of nano-structured ferritic alloy, *J. Nucl. Mater.* 377 (2008) 59–64, <https://doi.org/10.1016/j.jnucmat.2008.02.042>.
- [49] N. Cunningham, Y. Wu, D. Klingensmith, G.R. Odette, On the remarkable thermal stability of nanostructured ferritic alloys, *Mater. Sci. Eng.* 613 (2014) 296–305, <https://doi.org/10.1016/j.msea.2014.06.097>.
- [50] J.H. Schneibel, C.T. Liu, D.T. Hoelzer, M.J. Mills, P. Sarosi, T. Hayashi, U. Wendt, H. Heyse, Development of porosity in an oxide dispersion-strengthened ferritic alloy containing nanoscale oxide particles, *Scripta Mater.* 57 (2007) 1040–1043, <https://doi.org/10.1016/j.scriptamat.2007.07.029>.
- [51] R.L. Coble, A model for boundary diffusion controlled creep in polycrystalline materials, *J. Appl. Phys.* 34 (1963) 1679–1682, <https://doi.org/10.1063/1.1702656>.
- [52] W. Blum, X.H. Zeng, A simple dislocation model of deformation resistance of ultrafine-grained materials explaining Hall-Petch strengthening and enhanced strain rate sensitivity, *Acta Mater.* 57 (2009) 1966–1974, <https://doi.org/10.1016/j.actamat.2008.12.041>.
- [53] W. Blum, X.H. Zeng, Corrigendum to “A simple dislocation model of deformation resistance of ultrafine-grained materials explaining Hall-Petch strengthening and enhanced strain rate sensitivity” [1], *Acta Mater.* 59 (2011) 6205–6206, <https://doi.org/10.1016/j.actamat.2011.05.032>.
- [54] ASTM International, ASTM Standard E2627-13: Standard Practice for Determining Average Grain Size Using Electron Backscatter Diffraction (EBSD) in Fully Recrystallized Polycrystalline Materials, 2013.
- [55] D. Vaumousse, A. Cerezo, P.J. Warren, A procedure for quantification of precipitate microstructures from three-dimensional atom probe data, *Ultramicroscopy* 95 (2003) 215–221, [https://doi.org/10.1016/S0304-3991\(02\)00319-4](https://doi.org/10.1016/S0304-3991(02)00319-4).
- [56] A. Heinrich, T. Al-Kassab, R. Kirchheim, Investigation of the early stages of decomposition of Cu-0.7at.% Fe with the tomographic atom probe, *Mater. Sci. Eng.* 353 (2003) 92–98, [https://doi.org/10.1016/S0921-5093\(02\)00673-1](https://doi.org/10.1016/S0921-5093(02)00673-1).
- [57] E.A. Marquis, J.M. Hyde, Applications of atom-probe tomography to the characterisation of solute behaviours, *Mater. Sci. Eng. R Rep.* 69 (2010) 37–62, <https://doi.org/10.1016/j.mser.2010.05.001>.
- [58] E.A. Marquis, F. Vurpillot, Chromatic aberrations in the field evaporation behavior of small precipitates, *Microsc. Microanal.* 14 (2008) 561–570, <https://doi.org/10.1017/S1431927608080793>.
- [59] S.A. Danilkin, M. Hölzel, H. Fuess, H. Wipf, T.J. Udovic, J.J. Rush, V.E. Antonov, V. G. Gavriljuk, Crystal structure and lattice dynamics of hydrogen-loaded austenitic steel, *J. Phys. IV* 112 (2003) 407–410, <https://doi.org/10.1051/jp4:2003912>.
- [60] A. Benghalem, D.G. Morris, Milling and mechanical alloying of copper and some solution alloys seen as a thermomechanical process, *Acta Metall. Mater.* 42 (1994) 4071–4081, [https://doi.org/10.1016/0956-7151\(94\)90184-8](https://doi.org/10.1016/0956-7151(94)90184-8).
- [61] C. Oberdorfer, G. Schmitz, On the field evaporation behavior of dielectric materials in three-dimensional atom probe: a numeric simulation, *Microsc. Microanal.* 17 (2011) 15–25, <https://doi.org/10.1017/S1431927610093888>.
- [62] R. Peierls, The size of a dislocation, *Proc. Phys. Soc.* 52 (1940) 34–37, <https://doi.org/10.1088/0959-5309/52/1/305>.
- [63] F.R.N. Nabarro, Dislocations in a simple cubic lattice, *Proc. Phys. Soc.* 59 (1947) 256–272, <https://doi.org/10.1088/0959-5309/59/2/309>.
- [64] H.B. Huntington, Modification of the Peierls-Nabarro model for edge dislocation core, *Proc. Phys. Soc. B* 68 (1955) 1043–1048, <https://doi.org/10.1088/0370-1301/68/12/308>.
- [65] F.R.N. Nabarro, Theoretical and experimental estimates of the Peierls stress, *Philos. Mag. A* 75 (1997) 703–711, <https://doi.org/10.1080/01418619708207197>.
- [66] T. Suzuki, S. Takeuchi, Correlation of Peierls-Nabarro stress with crystal structure, *Rev. Phys. Appl.* 23 (1988), <https://doi.org/10.1051/rphysap:01988002304068500>, 685–685.
- [67] D.V. Kudashev, H. Baum, U. Martin, M. Heilmaier, H. Oettel, Microstructure and room temperature hardening of ultra-fine-grained oxide-dispersion strengthened copper prepared by cryomilling, *Mater. Sci. Eng.* 387–389 (2004) 768–771, <https://doi.org/10.1016/j.msea.2004.05.049>.
- [68] G. Dini, R. Uejji, A. Najafzadeh, S.M. Monir-Vaghefi, Flow stress analysis of TWIP steel via the XRD measurement of dislocation density, *Mater. Sci. Eng.* 527 (2010) 2759–2763, <https://doi.org/10.1016/j.msea.2010.01.033>.
- [69] A. Seeger, Peierls barriers, kinks, and flow stress: recent progress, *Z. Metallkd.* 93 (2002) 760–777, <https://doi.org/10.13139/146.020760>.

- [70] N. Zárubová, B. Šesták, Plastic deformation of Fe-3 wt% Si single crystals in the range from 113 to 473 K. I. Thermally activated plastic flow, *Phys. Status Solidi* 30 (1975) 365–374, <https://doi.org/10.1002/pssa.2210300138>.
- [71] H. Chen, A. Kauffmann, S. Laube, I.-C. Choi, R. Schwaiger, Y. Huang, K. Lichtenberg, F. Müller, B. Gorr, H.-J. Christ, M. Heilmaier, Contribution of lattice distortion to solid solution strengthening in a series of refractory high entropy alloys, *Metall. Mater. Trans.* 49 (2018) 772–781, <https://doi.org/10.1007/s11661-017-4386-1>.
- [72] I.-C. Choi, C. Brandl, R. Schwaiger, Thermally activated dislocation plasticity in body-centered cubic chromium studied by high-temperature nanoindentation, *Acta Mater.* 140 (2017) 107–115, <https://doi.org/10.1016/j.actamat.2017.08.026>.
- [73] M.M. Hutchison, The temperature dependence of the yield stress of polycrystalline iron, *Phil. Mag.: A Journal of Theoretical Experimental and Applied Physics* 8 (1963) 121–127, <https://doi.org/10.1080/14786436308212493>.
- [74] D.F. Stein, J.R. Low, Effects of orientation and carbon on the mechanical properties of iron single crystals, *Acta Metall.* 14 (1966) 1183–1194, [https://doi.org/10.1016/0001-6160\(66\)90236-7](https://doi.org/10.1016/0001-6160(66)90236-7).
- [75] R.L. Fleischer, Substitutional solution hardening, *Acta Metall.* 11 (1963) 203–209, [https://doi.org/10.1016/0001-6160\(63\)90213-X](https://doi.org/10.1016/0001-6160(63)90213-X).
- [76] W.F. Hosford, *Mechanical Behavior of Materials*, Cambridge University Press, Cambridge, 2005, p. 31.
- [77] P. Eckerlin, H. Kandler, Structure data of elements and intermetallic phases · Ac - Mn, in: K.-H. Hellwege, A.M. Hellwege (Eds.), *Structure Data of Elements and Intermetallic Phases*, Springer-Verlag, Berlin/Heidelberg, 1971, pp. 1–15, https://doi.org/10.1007/10201454_4.
- [78] G.I. Taylor, The mechanism of plastic deformation of crystals. Part I. Theoretical, *Proceedings of the Royal Society of London Series A* 145 (1934) 362–387, <https://doi.org/10.1098/rspa.1934.0106>.
- [79] H.J. Frost, M.F. Ashby, *Deformation-Mechanism Maps: the Plasticity and Creep of Metals and Ceramics*, Pergamon Press, Oxford, 1982, pp. 62–63.
- [80] H. Wiedersich, Hardening mechanisms and the theory of deformation, *J. Met.* 16 (1964) 425–430, <https://doi.org/10.1007/BF03398123>.
- [81] E.O. Hall, The deformation and ageing of mild steel: III Discussion of results, *Proc. Phys. Soc. B* 64 (1951) 747–753, <https://doi.org/10.1088/0370-1301/64/9/303>.
- [82] S. Takaki, K. Kawasaki, Y. Kimura, Mechanical properties of ultra fine grained steels, *J. Mater. Process. Technol.* 117 (2001) 359–363, [https://doi.org/10.1016/S0924-0136\(01\)00797-X](https://doi.org/10.1016/S0924-0136(01)00797-X).
- [83] B.P. Kashyap, Towards interrelationship of grain size, cell parameters and flow stress in type 316L stainless steel, *Acta Mater.* 50 (2002) 2413–2427, [https://doi.org/10.1016/S1359-6454\(02\)00073-3](https://doi.org/10.1016/S1359-6454(02)00073-3).
- [84] S. Rajasekhara, P.J. Ferreira, L.P. Karjalainen, A. Kyröläinen, Hall–Petch behavior in ultra-fine-grained AISI 301LN stainless steel, *Metall. Mater. Trans.* 38 (2007) 1202–1210, <https://doi.org/10.1007/s11661-007-9143-4>.
- [85] G.R. Odette, Recent progress in developing and qualifying nanostructured ferritic alloys for advanced fission and fusion applications, *J. Occup. Med.* 66 (2014) 2427–2441, <https://doi.org/10.1007/s11837-014-1207-5>.
- [86] M.C. Brandes, L. Kovarik, M.K. Miller, M.J. Mills, Morphology, structure, and chemistry of nanoclusters in a mechanically alloyed nanostructured ferritic steel, *J. Mater. Sci.* 47 (2012) 3913–3923, <https://doi.org/10.1007/s10853-012-6249-x>.
- [87] H. Oka, M. Watanabe, S. Ohnuki, N. Hashimoto, S. Yamashita, S. Ohtsuka, Effects of milling process and alloying additions on oxide particle dispersion in austenitic stainless steel, *J. Nucl. Mater.* 447 (2014) 248–253, <https://doi.org/10.1016/j.jnucmat.2014.01.025>.
- [88] M. Mabuchi, K. Higashi, Strengthening mechanisms of Mg-Si alloys, *Acta Mater.* 44 (1996) 4611–4618, [https://doi.org/10.1016/1359-6454\(96\)00072-9](https://doi.org/10.1016/1359-6454(96)00072-9).
- [89] B. Predel, Cr-Fe (Chromium-Iron), in: O. Madelung (Ed.), *Phase Equilibria, Crystallographic and Thermodynamic Data of Binary Alloys · Cr-Cs · Cu-Zr*, Springer-Verlag, Berlin/Heidelberg, 1994, pp. 1–10, https://doi.org/10.1007/10086090_973.
- [90] Scientific Group Thermodata Europe (SGTE), Ternary system Cr-Fe-Ni, in: P. Franke, H.J. Seifert (Eds.), *Ternary Steel Systems: Phase Diagrams and Phase Transition Data*, Springer-Verlag, Berlin/Heidelberg, 2012, pp. 386–400, https://doi.org/10.1007/978-3-540-88142-1_88.
- [91] J.P. Hirth, J. Lothe, in: *Theory of Dislocations*, 2nd, John Wiley & Sons, New York, 1982, p. 236.
- [92] B. Wilshire, T.D. Lieu, Deformation and damage processes during creep of Incoloy MA957, *Mater. Sci. Eng.* 386 (2004) 81–90, <https://doi.org/10.1016/j.msea.2004.07.047>.
- [93] G.R. Odette, M.J. Alinger, B.D. Wirth, Recent developments in irradiation-resistant steels, *Annu. Rev. Mater. Res.* 38 (2008) 471–503, <https://doi.org/10.1146/annurev.matsci.38.060407.130315>.
- [94] V.C. Nardone, J.K. Tien, Pinning of dislocations on the departure side of strengthening dispersoids, *Scripta Metall.* 17 (1983) 467–470, [https://doi.org/10.1016/0036-9748\(83\)90333-2](https://doi.org/10.1016/0036-9748(83)90333-2).
- [95] J.H. Schröder, E. Arzt, Weak beam studies of dislocation/dispersoid interaction in an ODS superalloy, *Scripta Metall.* 19 (1985) 1129–1134, [https://doi.org/10.1016/0036-9748\(85\)90022-5](https://doi.org/10.1016/0036-9748(85)90022-5).
- [96] J. Rösler, R. Joos, E. Arzt, Microstructure and creep properties of dispersion-strengthened aluminum alloys, *Metallurgical Transactions A* 23 (1992), <https://doi.org/10.1007/BF02647335>, 1521–1393.